Theoretical study of the geometries and decomposition energies of CO_2 on $Al_{12}X$: Doping effect of $Al_{12}X$

Jian-Ying Zhao [a,b], Feng-Qi Zhao [c], Si-Yu Xu [c], Xue-Hai Ju [a,*]

[a] Key Laboratory of Soft Chemistry and Functional Materials of MOE, School of Chemical Engineering, Nanjing University of Science and Technology, Nanjing 210094, PR China
[b] School of Chemistry and Chemical Engineering, Huaiyin Normal University, Huaian 223300, PR China
[c] Laboratory of Science and Technology on Combustion and Explosion, Xi'an Modern Chemistry Research Institute, Xi'an 710065, PR China

ARTICLE INFO

ABSTRACT

The adsorption and decomposition of CO_2 molecule on X-centered icosahedronal $Al_{12}X$ clusters (doping atom X = Al, Be, Zn, Fe, Ni, Cu, B, C, Si, P) were investigated by the DFT methods of PW91 and PWC. Adsorption energies, chemisorption energies and energy barriers of physic- and chemisorptions for CO_2 were determined. It was found that the doping atoms and spin states have important influences on the $Al_{12}X$ geometries, electronic properties and energies of the adsorption processes. CO_2 chemisorption on the $Al_{12}C$ cluster is energetically and kinetically unfavorable. CO_2 decomposition on the metallic doping $Al_{12}X$ (X = Fe, Ni, Cu) clusters has relatively low energy barriers. On contrary, the barriers are large when X = B, C, Si and P. The energy barriers for CO_2 chemisorption and decomposition on the $Al_{12}Fe$ cluster are 5.23 kJ/mol and 38.53 kJ/mol, respectively. These values are the lowest among all the clusters being discussed. The adsorption and decomposition of CO_2 on the $Al_{12}X$ cluster can be tuned by X doping.

© 2013 Elsevier Inc. All rights reserved.

1. Introduction

Aluminum particles are commonly used in solid rocket propellants, because of the large amounts of heat released during combustion [1,2]. Commonly used solid rocket propellants have little or no free oxygen content (often less than 1%) in their combustion products to react with the aluminum particles present [3]. Propellants with a hydroxy-terminated polybutadiene binder and an ammonium perchlorate oxidizer, such as that in the space shuttle solid rocket boosters, can contain up to 40–50% H_2O (g) and 10% CO_2 (depending on ammonium perchlorate content) within their combustion products [3,4]. Therefore, CO_2 acts as the dominant oxidizing species for the aluminum particles. For this reason, it is valuable to understand the behavior of Al powders in CO_2. In addition, new propulsion systems with metals burning in pure CO_2 have been recently proposed for sample return missions or Mars mobility [5,6]. Indeed, the Martian soil contains a significant proportion of Al, Mg, Si and Fe, and its atmosphere is composed of 95% CO_2. Thus, propulsion systems using these two natural resources have been proposed for the return to earth. Several studies have been performed over the past decades on the combustion of aluminum particles in pure CO_2 or in CO_2 containing mixtures. The Al–CO_2 combustion is checked as a result of the initial oxide layer that coats each particle [7–10]. Therefore, it is subjected to achieve high reactivity in aluminum in the Al–CO_2 reaction. One of the most effective ways to impart high reactivity to carbon dioxide is to use additives that, along with activated metal, form alloy or coat [11,12]. Schoenitz and Dreizin [13] and Shoshin et al. [14] investigated aluminum alloy on the basis of Mg or Ti reactivity with CO_2. They found the alloy leads to a higher reactivity in the Al–CO_2 reaction. However, many problems remain unsolved concerning the choice of the most cost effective alloy compositions that exhibit the maximal chemical activity at the same time. Additional, the Al burning in CO_2 is controlled by diffusion for particle sizes more than 200 μm, whereas for sizes less than 80 μm, the limiting step may be the kinetics of reactions on particle surface [3,4,6,15–18]. The experiment results of Bazyn et al. [19] showed that the 80 nm particles ignite at 1200 K. It indicated that the reaction mechanism at the different scale aluminum particles differs drastically. Such rapid nano-reaction cannot be explained by conventional mechanisms based on mass diffusion of reactants.

Because the burn rates of aluminum powders can be accelerated by reducing the size of Al particles. The applications of Al clusters can offer most desirable qualities of high heat release rates, extraordinary combustion efficiency, and tailored burning rate [20]. Among aluminum clusters, Al_{13} is a well-known magic cluster and its geometric structure is remarkably stable [21,22]. A recent study indicated that controllable X doping can tune electronic properties of $Al_{12}X$ clusters [23–26]. For example, substituting the central Al

* Corresponding author. Tel.: +86 25 84315947 801; fax: +86 25 84431622.
E-mail addresses: xhju@njust.edu.cn, juxuehai@eyou.com (X.-H. Ju).
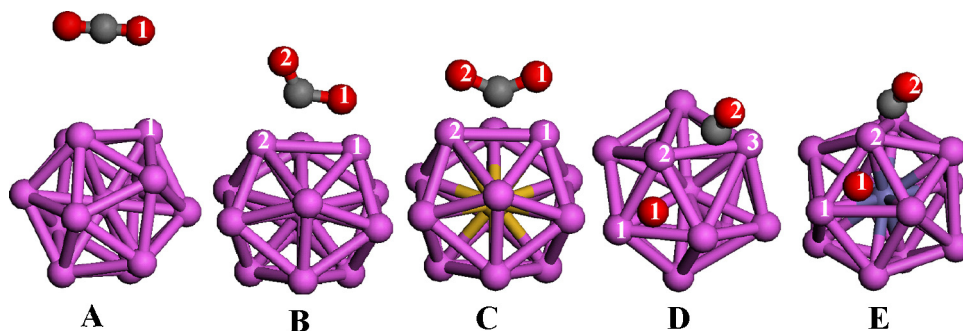
Fig. 1. Representative structures for physisorption configurations (A), chemisorption configurations (B and C), decomposition configurations (D and E) for two reaction paths considered in this work. Atom color code: purple, aluminum atoms; dark blue, iron atoms; red, oxygen.

atom of the icosahedral Al_{13} cluster by a pentavalent atom such as P or N would lead to a super alkali-metal atom of totally 41 valence electrons [27,28]; doped $Al_{12}B$ clusters exhibit the same characters of super halogen as Al_{13} [29].

Inspired by the activating capabilities of doped metal on aluminum clusters, we performed DFT computing for the interaction of CO_2 with a series of X-centered $Al_{12}X$ clusters (X = Al, Be, Zn, Ni, Fe, Cu, B, C, Si and P). The reaction energy and activation barrier for the CO_2 adsorption and decomposition were investigated. This would helpful for understanding different mechanisms with more enhanced reactivity than the larger particles. We found that the $Al_{12}X$ show distinctly different behaviors in adsorbing and dissociating CO_2 molecules, which might be useful for designing highly efficient reaction between Al and CO_2.

2. Computational methods

All the density functional theory calculations were performed using $Dmol^3$ [30,31] to derive equilibrium geometries, total energies, transition states and charge analysis. This method has been widely used in the theoretical calculations of clusters or X-doping systems [32,33]. Electronic exchange correlation was treated using two methods, local density approximation (LDA) with the PWC functional and generalized gradient approximation (GGA) with the PW91 functional [34,35]. The double zeta numerical basis sets including p- and d-polarization (DNP) [36,37] were employed, which are comparable to the Gaussian 6-31G (d, p) basis set in size and quality. In all $Dmol^3$ calculations, the all equilibrium geometries were optimized in a large cell of $14\text{Å} \times 14\text{Å} \times 14\text{Å}$. All the atomic positions in $Al_{12}X$ clusters were fully relaxed without any symmetry constraints. The convergence in energy, force and displacement were set to 10^{-5} Ha, 0.002 Ha/Å and 0.005 Å, respectively. A Fermi smearing of 0.136 eV and the real-space global orbital cutoff of 4.9 Å were used for these systems to accelerate SCF convergence. The quality mesh size for numerical integration was chosen. Transition state (TS) search was conducted using a combination of the linear synchronous transit and the quadratic synchronous transit methods (LST/QST) [38]. Vibrational frequency analysis was performed to characterize all stationary points as true minima or transition structures. TS optimization and TS confirmation calculations were performed to confirm that all transition structures were truly linked to the corresponding reactant and products. For all the systems studied, the spin-polarized calculations revealed that the low-spin state, that is, singlet for systems with even-number electrons and doublet for systems with odd-number electrons, are energetically preferable. For certainty, we also compared the energy differences of different spin multiplicities for $Al_{12}Fe$ and $Al_{12}Ni$ in Section 3.1.5. The chemisorption energies of CO_2 physi- and chemisorptions on $Al_{12}X$ clusters and the related activation barriers were corrected for the zero-point energies.

Due to the fact that the commonly used DFT methods neglect the dispersion or vdW interactions which play an important role in the adsorption geometry and energetics of adsorbed molecules, and intermolecular interactions as well [39–41], the dispersion correction scheme put forward by Ortmann, Bechstedt, and Schmidt (OBS) was adopted within DFT-D [42,43] for equilibrium geometries and energetics of physisorptions.

The basis set superposition error (BSSE) [44] exists in all quantum chemical calculations that deal with molecular interactions using finite basis sets. In some cases the BSSE may be so large as to completely mask the true molecular interaction [45]. The effects of basis set superposition error (BSSE) were fully removed using the following definition for adsorption energy E_{ads} in Eq. (1) [46]:

$$E_{ads} = E_{(CO_2+Al_{12}X)} - (E_{CO_2} + E_{Al_{12}X}) + E_{BSSE} \tag{1}$$

The activation energy is defined as follows:

$$E_a = E_{TS} - E_r \tag{2}$$

where $E_{(CO_2+Al_{12}X)}$ is the total energy of the relaxed $CO_2/Al_{12}X$ system after the CO_2 molecule was absorbed by the $Al_{12}X$ cluster, respectively. E_{CO_2} and $E_{Al_{12}X}$ are the total energies of the relaxed single CO_2 molecule and $Al_{12}X$ cluster, respectively. Hence, a negative E_{ads} value corresponds to stable adsorption on the cluster. E_{TS} is the energy of transition state, and E_r is the sum of the energies of reactants.

To verify our calculations, we compared results of Al_{13} with the available data. Fig. 1 shows the low energy configuration for the Al_{13} cluster using the PW91 functional. The nearest-neighbor distances lie in the range of 2.634–2.771 Å, 2.672–2.817 Å at the PWC, PW91 levels, respectively. It is found that the errors in the PW91 results are slightly smaller than those of the PWC results in comparison with the experimental values 2.618–2.958 Å [47] in the bulk system. At the PWC level, the C–O bond lengths are 1.168 Å and 1.174 Å for CO_2 and CO molecule, respectively. The corresponding values are 1.134 and 1.140 Å at the PW91 level, consistent with the experimental values of 1.16 and 1.128 Å. The PWC results are closer to the experimental values than PW91 results. However, the transition state (TS) can be easily searched by the PW91 (LST/QST). So, the following text on geometries and energetics was carried out by PW91. The results using PWC functionals were simply discussed. In addition, to verify calculations related to the spin states, we reoptimized their structures at the B3LYP/6-31G(d) level by using $Gaussian\ 03$ [48].

Based on the optimized geometries, the density of states (DOS) was obtained by Gaussian extension of the discrete energy levels, with weights being the orbital populations in the levels and the highest occupied molecular orbital (HOMO) as the Fermi level.

3. Results and discussion

3.1. Al$_{12}$X geometries, adsorption geometries, energetics

3.1.1. Al$_{12}$X geometries

The doped Al$_{12}$X clusters were obtained via replacing the central or surface atom of the icosahedral Al$_{13}$ cluster by Be, Zn, Fe, Ni, Cu, B, C, Si and P atom. The X-centered Al$_{12}$X clusters are more stable judged by the total energies. The following discussion concentrates on the X-centered Al$_{12}$X. The computed Al—Al bond lengths of outer Al$_{12}$ cage and Al—X bond lengths for the Al$_{12}$X clusters were listed in Table 1. The bond lengths between outer Al atoms and the central X atoms are slightly elongated by 0.000–0.010 Å for Al$_{12}$Si, Al$_{13}$, Al$_{12}$C and Al$_{12}$B, in agreement with earlier DFT calculations [23,49]. For all the selected elements, it can be found that the average value of the Al—Al bond length decreases in comparison with Al$_{13}$. The results show that doped atoms influence the geometries.

3.1.2. Physisorption geometries and energetics for CO$_2$ molecule on the Al$_{12}$X

When a CO$_2$ molecule approaches the Al$_{12}$X cluster, there are different starting configurations. The gas molecule can be located (orthogonal or parallel to the Al$_{12}$X) on top site, bridge site, a triangle site of Al. To ensure that the final converged configuration would be a global, rather than a local, minimum on the potential energy surface, all the possible configurations were selected as starting configurations. CO$_2$ physically adsorbs to triangular surface of Al$_{12}$X and forms State-I (Fig. 1). In State-I configurations, the C—O1 bond length increases slightly by about 0.000–0.003 Å, the OCO angle barely changes. The distance between O1 and Al1 atom ranges from 2.973 to 4.052 Å. These show that the interaction of CO$_2$ with Al$_{12}$X is of typical van der Waals.

The DFT-D correction adsorption energies ($E_{\text{ads-disp}} = E_{\text{ads}} + E_{\text{disp}}$) and adsorption energies (with the ZPE correction) (E_{ads}) are in the range of −19.86 to −10.28 kJ/mol and −12.97 to −3.48 kJ/mol, respectively. The dispersion interactions account for 30–78% of the adsorption energies. The dipole moments of Al$_{12}$X clusters have been changed from 0.0000 Debye into a range of 0.0038–0.0431 Debye. These also showed that the adsorption interaction is mostly a vdW interaction. From Table 1, the icosahedron structures of Al$_{12}$X are hardly affected by the physisorption of CO$_2$ molecule.

3.1.3. Chemisorption geometries and energetics for CO$_2$ molecule on the Al$_{12}$X

For the chemisorption of CO$_2$, similar starting configurations above-mentioned were applied to explore the most favorable chemisorption site. The only difference was that the starting distance between CO$_2$ and the Al$_{12}$X cluster was set smaller (1.9 Å) prior to the optimization. The optimized chemisorption structures (State-II) were in all clusters the same except Al$_{12}$Si, namely C—O1 bonds of the CO$_2$ molecule are located on the bridge (**B** in Fig. 1) with O1—Al1 bond length of 1.809–1.858 Å, and C—Al2 2.106–2.318 Å. In the Al$_{12}$Si (**C** in Fig. 1), the C atom locates on the bridge of the Al$_{12}$Si. The lengths of two Al—C bonds are 2.044 and 2.045 Å, and two Al—O bonds are 1.998 and 1.999 Å. CO$_2$ molecule is highly distorted. The OCO angle varies from 180° in State-I to 120.8–131.4° in State-II, the C—O1 bond lengths stretch from 1.174–1.177 to 1.280–1.367 Å, and C—O2 bond lengths stretch from 1.174–1.175 to 1.208–1.279 Å due to the bonding interactions. The electron density difference around the adsorption center of the Al$_{13}$ and Al$_{12}$Fe were also shown in Fig. 2. Electron clouds accumulate between O2 and Al1 atom to facilitate the Al—O bond formation. The electron depletion between C—O bond leads to the change in C—O bond order from two to one. Charge analysis shows that 0.54–0.57 electron transfers from the Al$_{12}$X clusters to the chemisorbed CO$_2$ of which the

Table 1
Geometrical parameters of Al$_{12}$, adsorption products, decomposition products of CO$_2$ on the Al$_{12}$X cluster at PW91/DNP level (bond: Å, angle:°).

Species	Bonds	Al$_{13}$	Al$_{12}$Be	Al$_{12}$Zn	Al$_{12}$Fe	Al$_{12}$Ni	Al$_{12}$Cu	Al$_{12}$B	Al$_{12}$C	Al$_{12}$Si	Al$_{12}$P
Al$_{12}$M	Al—Al	2.806–2.817	2.729–2.731	2.801–2.803	2.751–2.811	2.757–2.759	2.776–2.759	2.670–2.673	2.676–2.677	2.780–2.781	2.745–2.851
	Al—M	2.672–2.677	2.594–2.598	2.665–2.666	2.609–2.669	2.623–2.625	2.631–2.625	2.538–2.543	2.544–2.548	2.644–2.644	2.623–2.830
State-I	Al—Al	2.801–2.836	2.705–2.747	2.794–2.809	2.735–2.844	2.756–2.809	2.714–2.886	2.662–2.682	2.670–2.685	2.773–2.796	2.737–2.856
	Al—M	2.669–2.678	2.590–2.613	2.656–2.674	2.615–2.781	2.621–2.632	2.640–2.727	2.535–2.551	2.534–2.561	2.643–2.648	2.619–2.842
	Al1—O1	4.052	2.973	3.883	3.465	3.950	3.802	3.660	3.435	3.504	3.562
	C—O1	1.174	1.177	1.174	1.175	1.175	1.175	1.175	1.175	1.175	1.175
State-II	Al—Al	2.661–3.150	2.402–2.691	2.685–3.011	2.651–2.969	2.638–3.020	2.658–3.020	2.574–2.813	2.602–3.121	2.676–3.282	2.713–2.948
	Al—M	2.602–2.726	2.633–2.899	2.496–2.756	2.444–2.781	2.320–2.814	2.404–2.814	2.423–2.616	2.368–2.767	2.596–2.727	2.579–2.875
	Al1—O1	1.809	1.823	1.819	1.858	1.816	1.819	1.824	1.847	1.998	1.851
	Al2—C	2.110	2.106	2.112	2.318	2.115	2.157	2.122	2.172	2.045	2.178
	C—O1	1.356	1.354	1.357	1.334	1.367	1.342	1.342	1.322	1.280	1.337
	C—O2	1.213	1.213	1.213	1.208	1.213	1.213	1.215	1.220	1.279	1.218
	∠O—C—O	123.0	123.5	123.1	126.0	122.6	120.8	124.4	128.0	131.4	125.0
State-III	Al—Al	2.647–3.440	2.622–2.959	2.640–4.201	2.635–3.002	2.581–3.258	2.610–3.018	2.619–2.967	2.608–3.098	2.634–2.762	2.751–2.924
	Al—M	2.645–2.851	2.437–2.741	2.491–3.069	2.512–2.766	2.346–3.361	2.458–2.798	2.358–2.782	2.414–2.794	2.698–3.112	2.585–2.848
	Al—C	2.072–2.186	2.068–2.160	2.090–2.183	2.117	2.262–2.038	1.991	2.045–2.131	2.061	2.044	2.035
	C—O2	1.193	1.192	1.188	1.151	1.189	1.156	1.201	1.155	1.154	1.158

Table 2
Adsorption energy (E_{ads}), activation energies (E_a), chemisorption energies ($\Delta E_{chemisorp}$), and decomposition energies (E_{decomp}) of CO_2 adsorbing on the $Al_{12}X$ cluster at PW91/DNP (kJ/mol).

E	Al_{13}	$Al_{12}Be$	$Al_{12}Zn$	$Al_{12}Fe$	$Al_{12}Ni$	$Al_{12}Cu$	$Al_{12}B$	$Al_{12}C$	$Al_{12}Si$	$Al_{12}P$
E_{ads}	−10.51	−3.48	−12.97	−8.02	−10.59	−3.27	−8.31	−6.84	−4.32	−7.20
$E_{ads-disp}$	−19.38	−13.55	−19.86	−15.42	−17.43	−14.58	−17.41	−15.66	−18.25	−10.28
E_{a1}	38.09	17.33	37.48	5.23	25.15	24.79	33.48	44.30	47.00	25.85
$\Delta E_{chemisorp}$	−29.94	−62.38	−34.21	−24.41	−56.57	−47.49	−19.66	17.09	8.65	−11.91
E_{a2}	50.40	75.95	51.33	38.53	42.93	48.80	71.89	51.49	47.25	56.73
E_{decomp}	−37.61	−43.27	−54.26	−19.21	−92.39	−26.48	−34.35	−42.23	−34.36	−31.92

E_{a1} is chemisorption barrier, E_{a2} is decomposition barrier.
$\Delta E_{chemisorp}$ is total energy difference between physic- and chemi-sorption structures.

O1 atom acquires −0.21 to −0.24 e charge, O2 atom gains −0.032 to −0.039 e charge, while the C atom loses −0.3 e charge.

The chemisorption energy ($\Delta E_{chemisorp}$) was calculated by the total energy difference between State I and State II (a negative $\Delta E_{chemisorp}$ means exothermic). The results were collected in Table 2. From Table 2, CO_2 chemisorption on the $Al_{12}X$ clusters are exothermic as identified by the negative chemisorption energies (−62.38 to −11.91 kJ/mol) except $Al_{12}C$ and $Al_{12}Si$. The $Al_{12}X$ with doping metal exhibits relatively large chemisorption energies. The $Al_{12}Be$ has the largest chemisorption energy. On the contrary, the non-metal doped $Al_{12}X$ (X = B, P) have relatively low chemisorption energies.

The computed energy barriers (E_{a1}) between State-I and State-II were collected in Table 2. It also can be found that the energy barrier is lowered by the doped X (X = Be, Zn, Fe, Ni, Cu, B, P). The charge density of doped $Al_{12}X$ redistributes over the surface of the $Al_{12}X$ after CO_2 adsorbed. Calculation shows that the Mülliken charges of three Al atoms, on which CO_2 is adsorbed, are positive except that of Al_{13}. The doped X (X = Be, Zn, Fe, Ni, Cu, B, P) results in positive charge of adsorbed Al atoms, which increases electrostatic attraction between O1 atom and Al1 atom and reduces the barrier. For $Al_{12}C$ and $Al_{12}Si$ clusters, the energy barriers are heightened since the clusters have 40 valence electrons on the outside and are relatively stable. The energy barriers are relatively lower when X = Fe, Be, Zn, Ni and Cu, but larger when X = B, P, C and Si. The doped $Al_{12}Fe$ exhibits the lowest activation barrier (5.23 kJ/mol) and the barrier is less than the absolute value of the adsorption energy (−8.02 kJ/mol). This shows that CO_2 molecule easily chemisorbs to $Al_{12}Fe$. On the contrary, the doped $Al_{12}C$ and $Al_{12}Si$ are energetically and kinetically unfavorable for CO_2 chemisorptions.

3.1.4. Adsorption geometries and energetics for O atom and CO molecule on the $Al_{12}X$

To examine the decomposition of CO_2 on $Al_{12}X$ clusters, we defined the co-adsorption of CO and O (label: O2) dissociated from
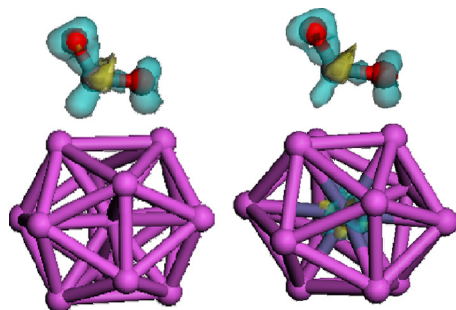
Fig. 2. Electron density difference of carbon dioxide chemisorption on Al_{13} (left) and $Al_{12}Fe$ (right). The isosurface cut-off value is 0.100 electrons/Å³. Cyan surface corresponds to charge accumulation, and yellow surface corresponds to charge depletion. Atom color code: purple, aluminum atoms; dark blue, iron atoms; red, oxygen atoms; Dark gray, carbon atoms. (For interpretation of the references to color in this figure legend, the reader is referred to the web version of the article.)

CO_2 on $Al_{12}X$ surface as State-III. The possible structures of State-III were displayed in Fig. 1D and E. As shown in Fig. 1, O2 atom lies on the triangle surface, there are two stable adsorption sites for CO. For X = Al, Be, Zn, Ni and B, CO molecule is approximately perpendicular to the bridge site, which is adjacent to the adsorbed O2 atom (Fig. 1D). For X = Fe, Cu, C, Si and P, CO molecule tilts to the top of Al atom (Fig. 1E). The computed structural parameters were listed in Table 1. It can be found that the C—Al distances are 1.991–2.186 Å and C—O2 lengths are 1.151–1.201 Å. Compared to isolated CO molecule, the C—O bonds are elongated by adsorbing interaction between CO molecule and $Al_{12}X$ clusters. Table 2 summarized the decomposition energy barriers (E_{a2}) and decomposition energy (E_{decomp}: the total energy difference between State II and State III). CO_2 decomposition on all $Al_{12}X$ clusters is exothermic. All the values of E_{a2} are larger than E_{a1}. The decomposition of CO_2 on $Al_{12}Fe$ still has the lowest energy barrier. For $Al_{12}Ni$, the chemisorption energy (−56.57 kJ/mol) can fully compensate for the decomposition barrier (E_{a2} = 42.93 kJ/mol). This shows that the chemisorbed CO_2 easily decomposes into CO and O atom on $Al_{12}Ni$. The decomposition of CO_2 on $Al_{12}Be$ cluster needs to overcome unusually large barriers. This may be due to the State-II of $Al_{12}Be$ is an exceptionally stable chemisorption configuration (the chemisorption energy is the largest among all the $Al_{12}X$ clusters).

3.1.5. Geometries, adsorption geometries and energetics of spin triplet $Al_{12}Ni$, and triplet and quintet $Al_{12}Fe$

For $Al_{12}Fe$, the energies of quintet and triplet states are only 1.21 and 2.89 kJ/mol over that of the singlet (Table 3). The energy of the triplet $Al_{12}Ni$ is 4.82 kJ/mol larger than that of its singlet state. According to the Boltzmann distribution formula, the proportion of the singlet, quintet and triplet spin state for $Al_{12}Fe$ is 52%, 36%, and 12%, respectively. These three states can be considered as energetically favorable low-lying states and coexist in same system. The triplet $Al_{12}Ni$, with 12% proportion, also coexists with the singlet state. Table 3 shows that the triplet $Al_{12}Fe$ deforms into an elongated icosahedron and the quintet a somewhat expanded icosahedron. The average values of the Al—Al and Al—X bond lengths of the triplet $Al_{12}Ni$ decrease in comparison with its singlet state. The results indicated that spin state of centered X affects the geometrical structure of $Al_{12}X$ cluster. As can be seen in Table 3, the E_{ads}, E_{a1}, E_{a2} and E_{decomp} have obvious differences between the singlet and other multiplicity states of $Al_{12}X$. The results indicate that the spin state of doped X can affect the geometries, adsorption geometries and energetics.

3.2. Performance of different exchange-correlation functionals

Since GGA is well known to overestimate the repulsion of van der Waals (vdW) interaction [50,51]. We have repeated the previous calculations using the LDA method. Compared to GGA, LDA performs well for the dispersion forces which are the main constituents of vdW interactions [52]. However, the LDA functional overestimates the attractive force of vdW complexes [53]. Hence

Table 3
Fundamental properties of $Al_{12}Fe$ and the interaction of $Al_{12}Fe$ with CO_2 for quintet and triplet spin state and $Al_{12}Ni$ for triplet spin state at PW91/DNP level.

Properties spin state	$Al_{12}Fe$			$Al_{12}Ni$	
	Singlet	Triplet	Quintet	Singlet	Triplet
ΔE (kJ/mol)	0.00	2.89	1.21	0.00	4.82
Al—X (Å)	2.619–2.676	2.611–2.689	2.624–2.670	2.623–.625	2.622–2.624
Al—Al (Å)	2.744–2.823	2.739–2.876	2.748–2.853	2.756–2.760	2.755–2.761
E_{ads} (kJ/mol)	−8.02	−8.39	−9.94	−10.59	−8.82
$E_{ads\text{-}disp}$ (kJ/mol)	−15.42	−15.59	−17.35	−17.43	−17.83
E_{a1} (kJ/mol)	5.23	3.25	14.49	25.12	25.90
$\Delta E_{chemisorp}$ (kJ/mol)	−24.41	−34.35	−28.29	−56.57	−47.27
E_{a2} (kJ/mol)	38.53	n.a.	n.a.	42.93	38.13
E_{decomp} (kJ/mol)	−34.25	−20.42	−12.02	−92.39	−46.53

ΔE is the energy difference between singlet and multiplicity.
n.a., the corresponding geometry is unconvergence at the PW91/DNP level.

Table 4
Adsorption energy (E_{ads}), activation energies (E_a), chemisorption energies ($\Delta E_{chemisorp}$), and decomposition energies (E_{decomp}) of CO_2 adsorbing on the $Al_{12}X$ cluster at PWC/DNP (kJ/mol).

E	Al_{13}	$Al_{12}Be$	$Al_{12}Zn$	$Al_{12}Fe$	$Al_{12}Ni$	$Al_{12}Cu$	$Al_{12}B$	$Al_{12}C$	$Al_{12}Si$	$Al_{12}P$
E_{ads}	−49.97	−44.72	−39.98	−26.82	−47.02	−37.80	−47.80	−40.95	−46.84	−43.06
$E_{ads\text{-}disp}$	−44.80	−52.79	−48.08	−33.40	−52.51	−45.81	−49.36	−51.08	−46.84	−50.87
E_{a1}	22.99	9.88	10.66	n.a.	2.36	3.00	16.61	30.66	31.81	3.04
$\Delta E_{chemisorp}$	−65.79	−91.69	−84.12	−88.26	−98.48	−73.41	−35.33	−1.72	−26.81	−47.70
E_{a2}	31.63	6.12	73.51	n.a.	28.12	48.92	31.37	50.15	63.73	63.99
E_{decomp}	−23.24	−63.36	−41.08	−28.57	−42.13	−56.99	−58.78	−34.23	−3.69	−31.77

E_{a1} is chemisorption barrier, E_{a2} is decomposition barrier.
n.a., the corresponding geometry is unconvergence at the PWC/DNP level.

the combination of GGA and LDA should reasonably bracket the correct behavior for the system, with the real adsorption energy lying between the values derived from these two methods. The computed results using PWC were collected in Table 4. Similar adsorption structures and transition states were observed from GGA: adsorption sites with similar configuration from previous calculation were identified. The geometry of $Al_{12}X$ is hardly changed in physisorption, the configurations deform more or less after chemisorption. A transition state is recognized to connect these two adsorption states. Comparing with GGA, the dispersion interactions account for 0.00–20% of the adsorption energies (Table 4). It can be found that the energy barriers (E_{a1}) are smaller and the adsorption energies are larger than that from the GGA method so that the State-I can easily turn into the State-II at LDA. This is understandable because LDA is known to underestimate reaction barrier heights owing to its overbinding effect [54]. Similarly, all the chemisorption energies calculated by LDA method are larger and the E_{a2} are generally lower than those predicted from GGA. And interestingly, the E_{a2} of $Al_{12}Zn$ is much larger than that from GGA, but $Al_{12}Be$ and $Al_{12}B$ are much lower than that from GGA, and the orders of energy changing (include E_{a1}, E_{a2}, E_{decomp}, E_{ads}) are not consistent with the GGA results. It may be due to the optimized geometries vary slightly with different computational levels such as GGA and LDA.

3.3. The density of states (DOS)

To probe into the controlling factors of adsorption, we turned our attention to angular-momentum resolved projected density of states (PDOS). We have plotted the PDOS for the free adsorbate, the outer Al_{12} cage of $Al_{12}X$, and outer Al_{12} cage of $Al_{12}X$ with adsorbate in the most stable configuration. Fig. 3 displayed the calculated partial DOS (PDOS) from −0.5 to 0.2 Ha for outer Al_{12} cages of $Al_{12}Fe$, $Al_{12}C$ and Al_{13}. From Fig. 3, we observed that there are distinct differences near the Fermi energy: PDOS of outer Al_{12} cage in Fermi energy level are from −0.067 to 0.043 Ha, −0.054 to 0.022 Ha and −0.032 to 0.022 Ha for $Al_{12}Fe$, $Al_{12}C$ and Al_{13}, respectively. The

numbers of peaks near Fermi level are 3, 2 and 1 for $Al_{12}Fe$, $Al_{12}C$ and Al_{13}, respectively. The DOS between −0.35 and −0.15 Ha have some similarities along with subtle differences for $Al_{12}Fe$ and Al_{13}. (Some peaks have shifted, e.g., the peak of −0.325 Ha shifted up to −0.30 Ha compared to Al_{13}.) The doped C introduces new peaks for s states of the surface Al atoms and some peaks shift. All these features indicate that the doped elements have an important effect on the delocalization of valence electrons states of outer Al_{12} cage, in agreement with Ref. [55]. Fig. 4 displayed PDOS from −0.5 to 0.2 Ha for outer Al_{12} cage of $Al_{12}Fe$ for singlet, triplet and quintet state. The PDOS of outer Al_{12} cage in Fermi energy level broaden (−0.066 to −0.044 Ha, −0.075 to −0.046 Ha, −0.075 to −0.054 Ha for singlet, triplet, quintet spin state, respectively) and some peaks shift with increasing multiplicity. The results show that the spin polarization of centered X atom also affects the delocalization of valence electrons states of outer atoms.
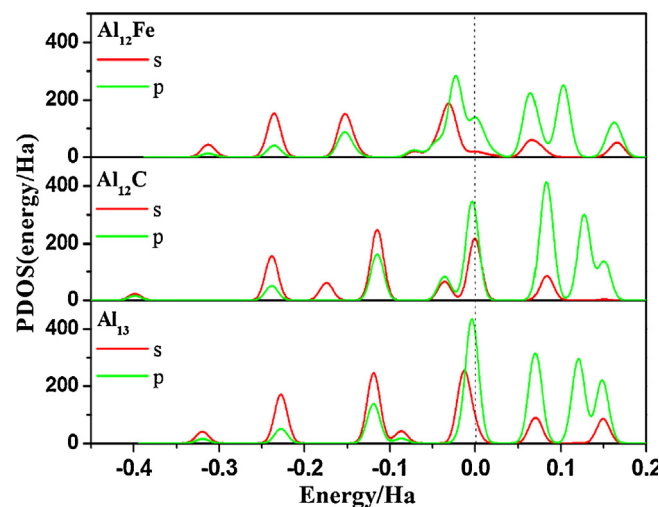
**Fig. 3.** The PDOS for the outer Al_{12} cage of Al_{13}, $Al_{12}C$ and $Al_{12}Fe$, respectively. The Fermi energy is set to zero.
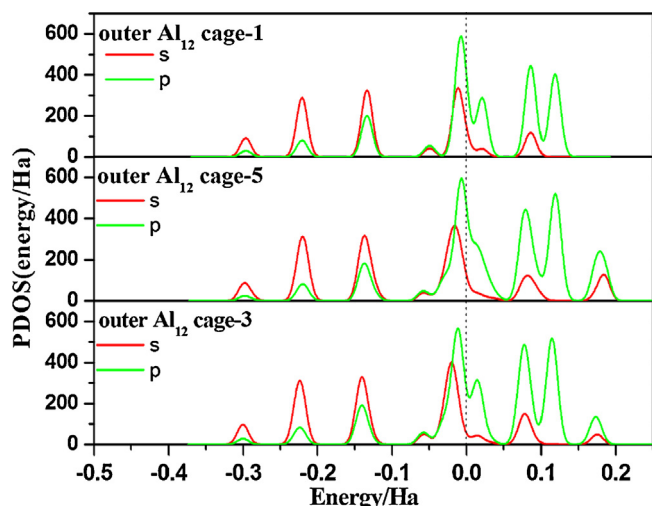
Fig. 4. The PDOS for the outer Al_{12} cage of $Al_{12}Fe$ for singlet (upper), quintet (middle) and triplet (lower) spin state, respectively.

Fig. 5 showed the calculated partial DOS (PDOS) from −0.45 to 0.25 Ha for CO_2 molecule physi-adsorbed on the $Al_{12}Fe$, $Al_{12}C$ and Al_{13}. For comparison, the PDOS for isolated CO_2 molecule and Al_{13}, $Al_{12}C$ and $Al_{12}Fe$ were also shown in Fig. 5. The PDOS of the isolated CO_2 clearly shows the positions of the three highest occupied molecular orbitals (HOMO) $1\pi_u$, $3\sigma_u$ and $1\pi_g$, and the lowest unoccupied molecular orbital (LUMO) $2\pi_u^*$. For State-I of $Al_{12}Fe$, one can clearly see from Fig. 6 that after adsorption, these three HOMOs shift down ca. 0.01 Ha. The PDOS of the outer cage near the Fermi energy broadens and the peak intensity decreases. Compared to the isolated CO_2 molecule, the distortion of the adsorbed CO_2 is very small (Table 1). Hence, these shifts of energy and decreased intensity can be attributed to the vdW interactions with the substrate. For State-I of $Al_{12}C$ and Al_{13}, three MOs of CO_2 molecule shift down 0.002 to 0.003 Ha. The peak intensity of the PDOS near the Fermi energy of the outer Al_{12} cage also decreases. These results indicated that the doping X element influences the CO_2–Al interaction as well as the CO_2 configuration. From Fig. 5 and Table 2, it can be found that the lower the energy for the MOs of adsorbed CO_2, the larger the E_{a1} values.

Fig. 6 shows the calculated PDOS from −0.45 to 0.20 Ha for State-II configurations of Al_{13}, $Al_{12}Fe$ and $Al_{12}C$. It can be seen that the $1\pi_g$ state of CO_2 shifts down in energy, overlaps with the 3s and 3p states of the underlying Al atom, and changes into broad bands. The peak intensity of $3\sigma_u$ state remarkably decreases. The $1\pi_u$ states remain nearly chemically inert (since its peak positions are practically unchanged). The low unoccupied molecular orbital (LUMO) $2\pi_u^*$ shifts from the empty band to around −0.1 Ha and Fermi level, compared to the State-I. It is obvious that the initially empty CO_2–$2\pi_u^*$ state has been populated by the s and p states of Al atoms. The population of the CO_2–$2\pi_u^*$ state being overlapped by the Al 3s and 3p electrons is the origin of O—C—O bending and C—O1 bond lengthening. These are accord with the results of Ref. [56].

The PDOS of State-III for Al_{13}, $Al_{12}C$ and $Al_{12}Fe$ were illustrated in Fig. 7. It can be found that HOMO orbital (5σ) of CO molecule overlaps with the 3s and 3p states of the underlying Al atoms and changes into broad band. The 5σ band in State-III of Al_{13} is broader than that of $Al_{12}C$, but the 5σ band of State-III $Al_{12}Fe$ hardly changes. This shows there is strong interaction between 5σ orbital and the 3s/3p states of the underlying Al atoms in Al_{13} State-III, but weak interaction in the State-III $Al_{12}Fe$. The LUMO orbital ($2\pi^*$) of CO shifts from the empty band to Fermi level and overlaps with the 3s, 3p states of the underlying Al atoms and changes into very broad band in State-III of Al_{13} and $Al_{12}Fe$, particularly in Al_{13}. In
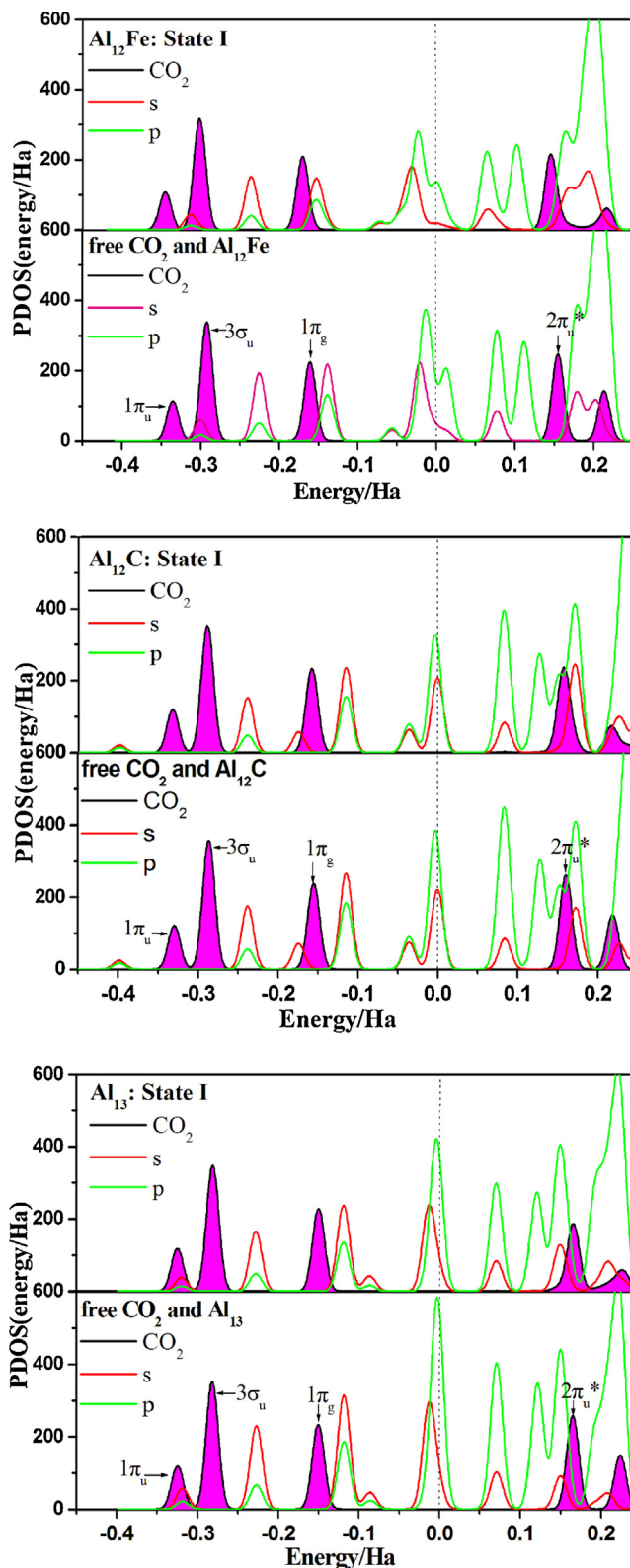
Fig. 5. The PDOS for CO_2 molecule of the physical adsorption and the outer Al_{12} cage. The area filled with magenta color represents molecular orbital of CO_2. The Fermi energy is set to zero. (For interpretation of the references to color in this figure legend, the reader is referred to the web version of the article.)

Table 5
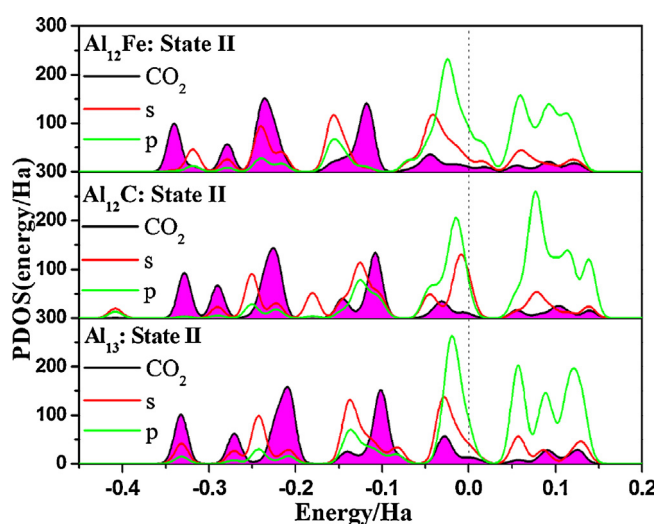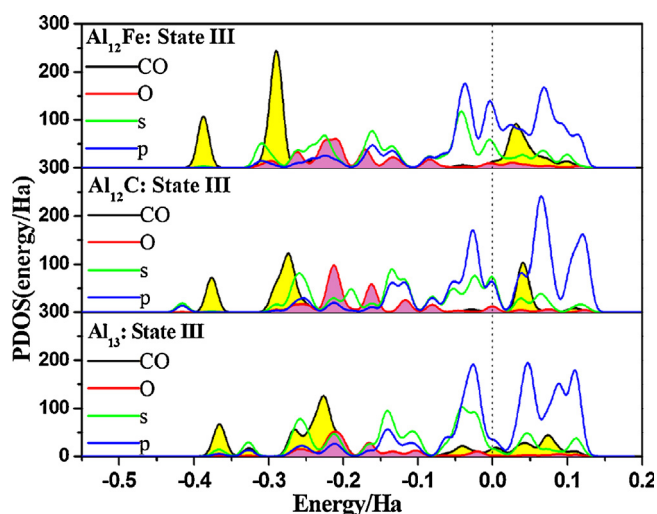The energy differences (ΔE in kJ/mol) between X-centered and surface X-replaced $Al_{12}X$ at PW91/DNP level.

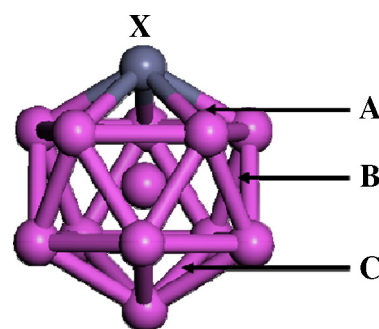| Energies	$Al_{12}Be$	$Al_{12}Zn$	$Al_{12}Fe$	$Al_{12}Ni$	$Al_{12}Cu$	$Al_{12}B$	$Al_{12}C$	$Al_{12}Si$	$Al_{12}P$
ΔE	126.50	21.10	11.37	125.90	79.58	227.20	248.34	62.47	18.87

Table 6
Adsorption energy (E_{ads}), activation energies (E_a), chemisorption energies ($\Delta E_{chemisorp}$), and decomposition energies (E_{decomp}) of CO_2 adsorbing on the surface X-replaced $Al_{12}X$ cluster at PW91/DNP (kJ/mol).

E	$Al_{12}Be$	$Al_{12}Zn$	$Al_{12}Fe$	$Al_{12}Ni$	$Al_{12}Cu$	$Al_{12}B$	$Al_{12}C$	$Al_{12}Si$	$Al_{12}P$
E_{ads}	−46.10	−34.14	−35.01	−64.29	−51.26	−68.78	−140.4	−32.88	−35.47
$E_{ads-disp}$	−54.20	−40.43	−25.52	−70.09	−49.44	−75.63	−147.3	−41.49	−40.76
E_{a1}	n.a.	41.47	n.a.	n.a.	n.a.	36.71	n.a.	40.89	50.51
$\Delta E_{chemisorp}$	−21.11	−17.77	−10.91	−87.26	−72.89	−110.2	−122.5	−20.11	−2.29
E_{a2}	1.78	10.29	14.67	16.26	n.a.	22.75	0.68	45.52	4.45
E_{decomp}	−159.77	−77.64	−218.66	−146.01	−78.82	−67.45	−18.89	−5.77	−82.34

E_{a1} is chemisorption barrier, E_{a2} is decomposition barrier.
n.a., the corresponding geometry is unconvergence at the PW91/DNP level.

Fig. 6. The PDOS for the CO_2 molecule of the chemisorption and the outer Al_{12} cage. The area filled with magenta color represents molecular orbital of CO_2. The Fermi energy is set to zero. (For interpretation of the references to color in this figure legend, the reader is referred to the web version of the article.)

Fig. 8. Adsorption sites of the surface X-replaced $Al_{12}X$.

$Al_{12}C$, $2\pi^*$ hardly changes. We found that the PDOS of State-III, in which the CO bonds to the bridge of $Al_{12}X$, is similar to Al_{13}. The PDOS of State-III $Al_{12}Cu$ is similar to $Al_{12}Fe$. These indicate that PDOS of State-III depends on the doped X.

3.4. Surface X-replaced $Al_{12}X$ adsorption geometries, energetics

The interaction of CO_2 with surface X-replaced $Al_{12}X$ was also investigated. The results were collected in Table 5. It can be found from Fig. 8 that there are three possible adsorption sites, i.e., **A**, **B** and **C** triangle sites. Only the adsorption configuration with the lowest energy was discussed for each species. The adsorption energy at **A** site is the largest for $Al_{12}X$ (X = Fe, B, Ni, Cu, Be) (Table 6), For $Al_{12}C$ and $Al_{12}Si$, the adsorption energies at **C** site are the largest. For $Al_{12}P$, CO_2 at **B** site is the largest. From Tables 2 and 6, it can be found that the adsorption energies are larger than those of X-centered clusters. The larger the energy differences between the X-centered and surface X-replaced $Al_{12}X$, the higher the adsorption energies. CO_2 chemisorption on the surface C and Si-replaced $Al_{12}X$ clusters is exothermic, but on the C and Si-centered ones are endothermic. From physic- and chemi-sorptions to decomposition for CO_2, the totally released energy on the surface X-replaced $Al_{12}X$ are generally larger than on the X-centered $Al_{12}X$. Unfortunately, we failed to locate the TS1 for most $Al_{12}X$ clusters. The energy barriers (E_{a1}) are higher than that on the X-centered $Al_{12}X$. However, the E_{a2} are lower than that on the X-centered $Al_{12}X$.

4. Conclusions

In this work we have performed first principle calculations on the adsorption of CO_2 on neutral X-centered icosahedronal $Al_{12}X$ clusters (X = Be, Zn, Fe, Ni, Cu, B, C, Si and P). It has been found that

Fig. 7. The PDOS for the CO, O and the outer Al_{12} cage. The area filled with yellow color represents orbital of CO molecule and LT magenta color represents orbital of O atom. The Fermi energy is set to zero. (For interpretation of the references to color in this figure legend, the reader is referred to the web version of the article.)

the doping atoms and its spin states have important influences on the $Al_{12}X$ geometries. Compared with Al_{13}, the bond lengths between surface Al atoms and the central X atoms are shortened. Further more, the doping elements and its spin states have an important effect on the delocalization of valence electrons states of outer cage atoms.

The almost horizontal CO_2 molecule tends to physi-adsorb on the triangle surface of the $Al_{12}X$. Judged by the PDOS of $Al_{12}X$ physisorption configurations, the doping X elements influence the interaction between the adsorbed CO_2 and the substrate Al atom. The lower the MOs energies of the adsorbed CO_2 are, the lower the energy barriers for transferring the State-I to State-II are. The chemisorption of CO_2 on $Al_{12}X$ clusters can be tuned by controllable doping. Among the $Al_{12}X$ clusters being considered, the transition from a physisorbed to a chemisorbed complex of CO_2 shows a relatively low energy barrier for the metal doped $Al_{12}X$, but relatively high energy barriers for non-metal doped analogs. $Al_{12}Fe$ clusters exhibit the lowest energy barrier, and is thermodynamically favorable and kinetically accessible for CO_2 adsorption.

CO_2 decomposition on doping $Al_{12}X$ clusters also can be tuned by controllable X doping and has been found to form two kinds of equilibrium structures. The CO_2 decomposition on the doped $Al_{12}Fe$ cluster has lowest activation barriers. For $Al_{12}Ni$, the chemisorption energy can fully compensate for the energy barrier for CO_2 decomposition.

The adsorption of CO_2 on surface X-replaced $Al_{12}X$ clusters was also calculated. It was found that the surface X-replaced $Al_{12}X$ clusters are more reactive than the X-centered ones. The adsorption energies of the formers are larger than that of the X-centered clusters.

The variation of chemisorption energy and energy barrier for chemisorbed CO_2 with doping X suggests that an efficient $Al_{12}X$ clusters can be screened out. The doped $Al_{12}X$ clusters can be served as highly efficient and low-cost reagents for carbon dioxide activation and decomposition.

Acknowledgments

References

[1] B. Palaszewski, L.S. Ianovski, P. Carrick, Propellant technologies: far-reaching benefits for aeronautical and space-vehicle propulsion, J. Propul. Power 14 (1998) 641–648.

[2] F. Zhang, S.B. Murray, K.B. Gerrard, Aluminum particles–air detonation at elevated pressures, Shock Waves 15 (2006) 313–324.

[3] J. Servaites, H. Krier, J.C. Melcher, R.L. Burton, Ignition and combustion of aluminum particles in shocked $H_2O/O_2/Ar$ and $CO_2/O_2/Ar$ mixtures, Combust. Flame 125 (2001) 1040–1054.

[4] V. Sarou-Kanian, J.C. Rifflet, F. Millot, I. Gökalp, Aluminum combustion in wet and dry CO_2: consequences for surface reactions, Combust. Flame 145 (2006) 220–230.

[5] E. Shafirovich, A. Varma, Metal–CO_2 propulsion for mars missions: current status and opportunities, J. Propul. Power 24 (2008) 385–394.

[6] V. Sarou-Kanian, J.C. Rifflet, F. Millot, E. Veron, T. Sauvage, I. Gökalp, On the role of carbon dioxide in the combustion of aluminum droplets, Combust. Sci. Technol. 177 (2005) 2299–2326.

[7] S.A. Rashkovsky, Metal agglomeration in solid propellants combustion, Combust. Sci. Technol. 136 (1998) 125–148.

[8] S. Yuasa, S. Sogo, H. Isoda, Ignition and combustion of aluminum in carbon dioxide streams, in: Twenty-Fourth Symposium (International) on Combustion, vol. 24, The Combustion Institute, Pittsburgh, 1992, pp. 1817–1825.

[9] J.C. Melcher, R.L. Burton, H. Krier, Burning aluminum particles inside a laboratory-scale solid rocket motor, J. Propul. Power 18 (2002) 631–640.

[10] V. Sarou-Kanian, J.C. Rifflet, F. Millot, G. Matzen, I. Gökalp, Influence of nitrogen in aluminum droplet combustion, Proc. Combust. Inst. 30 (2004) 2060–2067.

[11] M. Schoenitz, E.L. Dreizin, E. Shtessel, Constant volume explosions of aerosols of metallic mechanical alloys and powder blends, J. Propul. Power 19 (2003) 405–412.

[12] T.A. Andrzejak, E. Shafirovich, A. Varma, Ignition mechanism of nickel-coated aluminum particles, Combust. Flame 150 (2007) 60–70.

[13] M. Schoenitz, E.L. Dreizin, Oxidation processes and phase changes in metastable Al–Mg alloys, J. Propul. Power 20 (2004) 1064–1068.

[14] Y.L. Shoshin, M.A. Trunov, X. Zhu, M. Schoenitz, E.L. Dreizin, Ignition of aluminum-rich Al:Ti mechanical alloys in air, Combust. Flame 144 (2006) 688–697.

[15] B. Legrand, M. Marion, C. Chauveau, I. Gökalp, E. Shafirovich, Ignition and combustion of levitated magnesium and aluminum particles in carbon dioxide, Combust. Sci. Technol. 165 (2001) 151–174.

[16] S. Rossi, E.L. Dreizin, C.K. Law, Combustion of aluminum particles in carbon dioxide, Combust. Sci. Technol. 164 (2001) 209–237.

[17] N. Glumac, H. Krier, T. Bazyn, R. Eyer, Temperature measurements of aluminum particles burning in carbon dioxide, Combust. Sci. Technol. 177 (2005) 485–511.

[18] T. Bazyn, H. Krier, N. Glumac, Evidence for the transition from the diffusion-limit in aluminum particle combustion, Proc. Combust. Inst. 31 (2007) 2021–2028.

[19] T. Bazyn, H. Krier, N. Glumac, Combustion of nanoaluminum at elevated pressure and temperature behind reflected shock waves, Combust. Flame 145 (2006) 703–713.

[20] J.K. Pamela, M.R. Betsy, Novel energetic materials for the future force: the army pursues the next generation of propellants and explosives, AMPTIAC Q. 8 (2004) 85–89.

[21] K.J. Taylor, C.L. Pettiette, M.J. Craycraft, O. Chesnovsky, R.E. Smalley, Ups of negative aluminum clusters, Chem. Phys. Lett. 152 (1988) 347–352.

[22] Z.G. Zhang, H.G. Xu, Y. Feng, W.J. Zheng, Investigation of the superatomic character of Al_{13} via its interaction with sulfur atoms, J. Chem. Phys. 132 (2010) 161103–161104.

[23] L. Wang, J. Zhao, Z. Zhou, S.B. Zhang, Z. Chen, First-principles study of molecular hydrogen dissociation on doped $Al_{12}X$ (X = B, Al, C, Si, P, Mg, and Ca) clusters, J. Comput. Chem. 30 (2009) 2509–2514.

[24] A. Nakajima, T. Kishi, T. Sugioka, K. Kaya, Electronic and geometric structures of aluminum-boron negative cluster ions ($Al_nB_m^-$), Chem. Phys. Lett. 187 (1991) 239–244.

[25] P. Jena, A.W. Castleman Jr., Clusters: a bridge across the disciplines of physics and chemistry, Proc. Natl. Acad. Sci. U.S.A. 103 (2006) 10560–10569.

[26] D.J. Henry, I. Yarovsky, Dissociative adsorption of hydrogen molecule on aluminum clusters: effect of charge and doping, J. Phys. Chem. A 113 (2009) 2565–2571.

[27] M. Akutsu, K. Koyasu, J. Atobe, N. Hosoya, K. Miyajima, M. Mitsui, A. Nakajima, Experimental and theoretical characterization of aluminum-based binary superatoms of $Al_{12}X$ and their cluster salts, J. Phys. Chem. A 110 (2006) 12073–12076.

[28] B.L. Wang, J.J. Zhao, D.N. Shi, X.S. Chen, G.H. Wang, Density-functional study of structural and electronic properties of $Al_nN(n=2-12)$ clusters, Phys. Rev. A 72 (2005) 023204–023205.

[29] X.G. Gong, V. Kumar, Enhanced stability of magic clusters: a case study of icosahedral $Al_{12}X$, X = B, Al, Ga, C, Si, Ge, Ti, As, Phys. Rev. Lett. 70 (1993) 2078–2081.

[30] B. Delley, An all-electron numerical-method for solving the local density functional for polyatomic-molecules, J. Chem. Phys. 92 (1990) 508–517.

[31] B. Delley, From molecules to solids with the Dmol^3 approach, J. Chem. Phys. 113 (2000) 7756–7764.

[32] A. Deka, R.C. Deka, A density functional study on equilibrium geometries, stabilities and electronic properties of Au_5Li binary clusters, Appl. Nanosci. 2 (2012) 359–364.

[33] J. Du, X. Sun, J. Chen, G. Jiang, A theoretical study on small iridium clusters: structural evolution, electronic and magnetic properties, and reactivity predictors, J. Phys. Chem. A 114 (2010) 12825–12833.

[34] Y. Liu, Y. Hua, M. Jiang, G. Jiang, J. Chen, Theoretical study of the geometries and dissociation energies of molecular water on neutral aluminum clusters Al_n ($n=2-25$), J. Chem. Phys. 136 (2012) 084703–084709.

[35] J.P. Perdew, Y. Wang, Accurate and simple analytic representation of the electron-gas correlation energy, Phys. Rev. B 45 (1992) 13244–13249.

[36] J.P. Perdew, K. Burke, M. Ernzerhof, Generalized gradient approximation made simple, Phys. Rev. Lett. 77 (1996) 3865–3868.

[37] C.T. Lee, W.T. Yang, R.G. Parr, Development of the Colle–Salvetti correlation-energy formula into a functional of the electron-density, Phys. Rev. B 37 (1988) 785–789.

[38] T.A. Halgren, W.N. Lipscomb, The synchronous-transit method for determining reaction pathways and locating molecular transition states, Chem. Phys. Lett. 49 (1977) 225–232.

[39] K.E. Riley, M. Pitoňák, P. Jurečka, P. Hobza, Stabilization and structure calculations for noncovalent interactions in extended molecular systems based on wave function and density functional theories, Chem. Rev. 110 (2010) 5023–5063.

[40] P. Hobza, R. Zahradnik, K. Müller-Dethlefs, The world of non-covalent interactions, Collect. Czech. Chem. Commun. 71 (2006) 443–531.

[41] L. Goerigk, S. Grimme, A thorough benchmark of density functional methods for general main group thermochemistry, kinetics, and noncovalent interactions, Phys. Chem. Chem. Phys. 13 (2011) 6670–6688.

[42] S. Grimme, Accurate description of van der Waals complexes by density functional theory including empirical corrections, J. Comput. Chem. 25 (2004) 1463–1473.

[43] S. Grimme, Density functional theory with London dispersion corrections, WIREs Comput. Mol. Sci. 1 (2011) 211–228.

[44] E.R. Davidson, S.J. Chakravarty, Reply to comment on "a possible definition of basis set superposition error", Chem. Phys. Lett. 241 (1995) 146–148.

[45] F. Jensen, The magnitude of intramolecular basis set superposition error, Chem. Phys. Lett. 261 (1996) 633–636.

[46] H.K. Kyung, K. Yongho, The basis set superposition error in multilevel methods: a test on the H_2O and HF dimer, Theor. Chem. Acc. 115 (2006) 18–26.

[47] O. Tougait, H. Noel, Stoichiometry of UAl_4, Intermetallics 12 (2004) 219–223.

[48] GAUSSIAN 03, Revision C.02, Gaussian Inc., Wallingford, CT, 2003.

[49] S.N. Khanna, P. Jena, Assembling crystals from clusters, Phys. Rev. Lett. 69 (1992) 1664–1667.

[50] A. Singh, A. Sen, B. Ganguly, First principle study towards the influence of Cd^{2+} on the morphology of sodium chloride, J. Mol. Graphics Modell. 28 (2010) 413–419.

[51] F.O. Kannemann, A.D. Becke, Van der Waals interactions in density-functional theory: rare-gas diatomics, J. Chem. Theory Comput. 5 (2009) 719–727.

[52] G. Saranya, S. Nair, V. Natarajan, P. Kolandaivel, K. Senthilkumar, A theoretical study of structural and electronic properties of pentacene/Al(1 0 0) interface, J. Mol. Graphics Modell. 38 (2012) 334–341.

[53] T. Sato, T. Tsuneda, K. Hirao, Long-range corrected density functional study on weakly bound systems: balanced descriptions of various types of molecular interactions, J. Chem. Phys. 126 (2007) 234114–234212.

[54] S. Andersson, M. Grüning, Performance of density functionals for calculating barrier heights of chemical reactions relevant to astrophysics, J. Phys. Chem. A 108 (2004) 7621–7636.

[55] M.X. Chen, X.H. Yan, S.H. Wei, Al_7Ag and Al_7Au clusters with large highest occupied molecular orbital-lowest unoccupied molecular orbital gap, J. Phys. Chem. A 111 (2007) 8659–8662.

[56] R. Atta-Fynn, A.K. Ray, A first principles study of the adsorption and dissociation of CO_2 on the δ-Pu(1 1 1) surface, Eur. Phys. J. B 70 (2009) 171–184.